Combining two-photon lithography with laser ablation of sacrificial layers: A route to isolated 3D magnetic nanostructures

Arjen van den Berg[1], Mylène Caruel[2], Matthew Hunt[1], and Sam Ladak[1] (✉)

[1] School of Physics and Astronomy, Cardiff University, Cardiff, CF24 3AA, UK
[2] Institut National des Sciences Appliquées (INSA) of Toulouse, 35 Avenue de Rangueil, 31400 Toulouse, France

ABSTRACT

Three-dimensional (3D) nanostructured functional materials are important systems allowing new means for intricate control of electromagnetic properties. A key problem is realising a 3D printing methodology on the nanoscale that can yield a range of functional materials. In this article, it is shown that two-photon lithography, when combined with laser ablation of sacrificial layers, can be used to realise such a vision and produce 3D functional nanomaterials of complex geometry. Proof-of-principle is first shown by fabricating planar magnetic nanowires raised above the substrate that exhibit controlled domain wall injection and propagation. Secondly, 3D artificial spin-ice (3DASI) structures are fabricated, whose complex switching can be probed using optical magnetometry. We show that by careful analysis of the magneto-optical Kerr effect signal and by comparison with micro-magnetic simulations, depth dependent switching information can be obtained from the 3DASI lattice. The work paves the way for new materials, which exploit additional physics provided by non-trivial 3D geometries.

KEYWORDS

three-dimensional (3D) nanomagnetism, 3D lithography, 3D artificial spin ice, sacrificial layers, magneto-optical Kerr effect

1   Introduction

Three-dimensional (3D) printing of materials is proving to be an important technology, allowing rapid prototyping and manufacture of a range of physical systems across different length scales. Recent work has demonstrated multi-nozzle 3D printing in order to realise a number of multi-material systems, including robot walkers and intricate origami structures upon the macroscale [1]. The reduction of such processes to physically important length scales, particularly upon the nanoscale [2], enables the investigation of a range of exotic phenomena and associated applications. Examples include 3D nanostructured systems with outstanding mechanical properties [3, 4], systems with bespoke phononic bandgaps [5], frustrated magnetic nanowire lattices [6], controlled Hall coefficients in 3D chainmail metamaterials [7], and 3D conductive nanowires [8] allowing the production of coils and on-chip interconnects. A diverse range of methodologies are available for 3D printing upon the nanoscale, but each is usually tailored to producing a limited type of material, making the realisation of more complex systems that rely upon multiple functional materials difficult [2].

A methodology to cast the shell of a polymer-based 3D nanostructure into other functional materials would be an important development in materials science, allowing the production of bespoke multifunctional materials. In order to obtain maximum benefit from such an approach, it should be compatible with conventional deposition processes allowing access to a wide range of metallic and dielectric materials with different functionalities. A key challenge with such an approach is ensuring the desired material only covers the relevant 3D nanostructure,

leaving the rest of the substrate clean. Recent review articles highlight the versatility of two-photon lithography (TPL) [9–11], yet there is a paucity of work demonstrating selective deposition or removal of functional materials upon nanostructures. Existing attempts in the literature use sacrificial structures to shadow regions and prevent deposition selectively [12, 13], but these have limited applicability for 3D geometries. Sacrificial layers enable the selective removal or deposition of functional materials upon nanostructures fabricated using TPL but are thus far unexplored in the literature.

The emerging field of 3D nanomagnetism [6, 10, 14–17] is an excellent example of how nanoscale control of 3D geometry can yield a range of new physical phenomena and advanced device concepts. Of particular note is the pioneering concept of magnetic racetrack systems [18, 19], which utilise domain walls within 3D nanowire systems in order to store information. 3D magnetic nanowires were recently realised in simple angled geometries using focussed electron beam lithography of Pt, followed by $Ni_{81}Fe_{19}$ evaporation [20]. A key problem with this approach was the presence of $Ni_{81}Fe_{19}$ sheet film upon the substrate, making it more difficult to probe the magnetism of the nanowires. This obstacle was surpassed by an innovative dark-field optical magnetometry technique, which allowed the switching of such wires to be determined. In general, probing the switching of more complex 3D magnetic nanostructures is difficult if a background sheet film is present since it produces a large signal in the magnetometry, which can overpower any more subtle signals from structures. In this article, we propose a method to solve this problem by combining laser ablation of sacrificial layers with 3D

lithography in order to realise 3D magnetic nanostructures with no background sheet film. Proof-of-principle is demonstrated by fabricating lone magnetic nanowires raised above the substrate and with domain wall nucleation pads, opening up new avenues for the fundamental study of 3D magnetic nanowires. Furthermore, we demonstrate that the technique can be harnessed to study magnetometry in more complex 3D artificial spin-ice (3DASI) structures.

A key challenge in realising such a process is identifying a sacrificial layer that can be ablated at high-resolution with femtosecond laser exposure, remains chemically stable during the TPL development process, and can then be finally removed in such a way that the 3D structures remain intact. We note that conventional photoresists are not suitable since they are removed or damaged during the development of 3D structures which utilise the solvent propylene glycol monomethyl ether acetate (PGMEA). We have identified polyacrylic acid (PAA) as satisfying the relevant criteria. Crucially, this high molecular weight polymer (inset of Fig. 1(a)) is chemically stable in the presence of commonly used solvents in lithography, such as PGMEA and isopropanol, but swells when immersed in water [21].

Figures 1(a)–1(h) show an overview of the fabrication process. The sacrificial layer, PAA, is first spun onto a glass substrate (Fig. 1(b)), after which trenches of the material are ablated away using high-resolution femtosecond laser machining (Fig. 1(c)). After ablation, a negative tone photoresist is drop-cast upon the sample (Fig. 1(d)), and the desired structure is written into the ablated trenches using TPL (Fig. 1(e)). Here the versatility of TPL can be used to produce any 3D geometry within the trench. The unexposed resist is removed by placing the sample in a PGMEA bath for 20 min, followed by an isopropyl alcohol (IPA) bath (Fig.
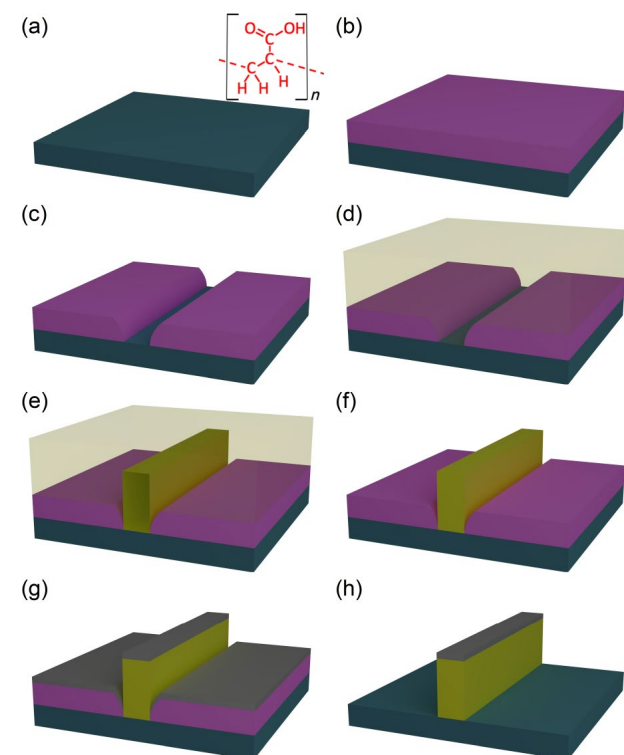
1(f)). Magnetic material ($Ni_{81}Fe_{19}$) is deposited using thermal evaporation (Fig. 1(g)), after which the PAA layer is lifted off in an aqueous sodium hydroxide (0.5 mol·L^{-1}) bath (Fig. 1(h)). A critical requirement for such a process is the well-controlled ablation of the PAA sacrificial layer. Our femtosecond laser ($\tau = 100$ fs, rep rate 80 MHz) operates in the infrared ($\lambda = 780$ nm), meaning there is insufficient energy to yield direct photolysis of carbon-based bonds within PAA. However, recent work has suggested that ultrafast lasers within the infrared can ablate polymers through multiphoton absorption [22].

2 Results and discussion

Single-voxel trenches were ablated into a PAA layer with varying laser power and scan speed to characterise the ablation process. The profile of each trench was measured using atomic force microscopy (AFM). A representative AFM image is shown in Fig 2(a) with a 3D rendered view of the data shown in Fig. 2(b).

A height profile of a typical trench is shown in Fig. 2(c). Shoulders on either side of the ablated region indicate that the ablation process is photothermal with laser exposure creating a melt pool as the PAA is heated. Subsequent exposure yields explosive vapourisation of the molten material. The recoil results in the molten material being ejected and redeposited upon surrounding areas [23]. The onset of uniform ablated lines starts at a power of approximately 50 mW, yielding feature sizes of below 300 nm, after which it increases with laser power (Fig. 2(d)). Below 50 mW, ablated lines appear non-uniform and could not be used to produce clear trenches for this process (Fig. S1 in the Electronic Supporting Material (ESM)). The depth of the ablated trench is shown in Fig. 2(e). Herein, it can be seen that the depth increases for low powers before saturating at the PAA film thickness.

To demonstrate the feasibility of our approach, we fabricate the simplest possible structures, that of $Ni_{81}Fe_{19}$ nanowires and nanowires with domain wall nucleation pads. In both cases, the nanowire is raised 3 μm above the substrate. A scanning electron

Figure 1 Outline of the Fabrication process. (a) A glass/ITO substrate is cleaned with acetone followed by IPA. (b) Polyacrylic acid is spin-coated onto the substrate. (c) Femtosecond laser machining is used to ablate the desired geometry into the PAA. (d) A negative tone photoresist is drop-cast upon the sample. (e) The desired 3D geometry is written into the polymer using two-photon lithography. (f) Unexposed resist is washed away using PGMEA. (g) $Ni_{81}Fe_{19}$ is deposited by evaporation. (h) The PAA is removed using deionised water and the substrate film is lifted off.
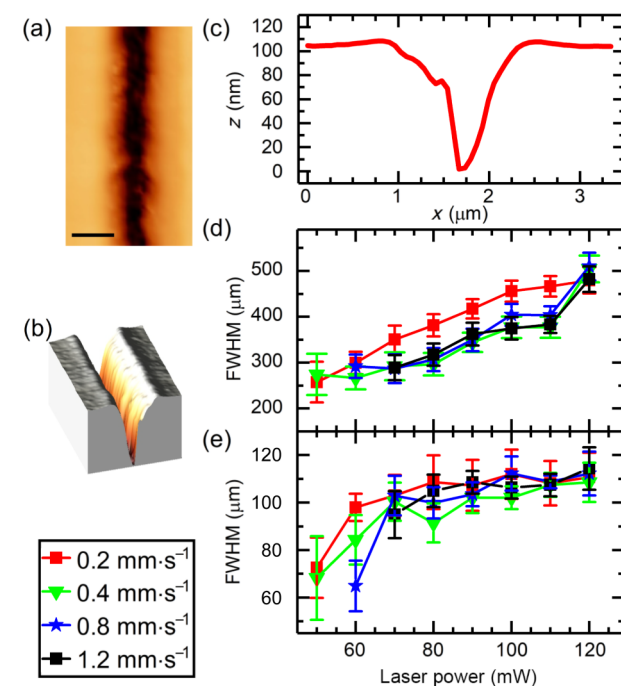

Figure 2 (a) Atomic force microscopy image of a single trench ablated into a polyacrylic acid layer. Scale bar indicates 500 nm. (b) 3D representation of ablated trench. (c) Height profile of typical trench. (d) Full-width at half maximum (FWHM) measurements of trenches as a function of laser power and scan speed. (e) Trench depth as a function of laser power and scan speed.

microscopy image of a nanowire with a nucleation pad is shown in Fig. 3(a).

The fabricated wires have a length of 100 μm and a width of 300 nm. The nucleation pad measured 20 μm × 20 μm. Elemental maps were captured using energy dispersive X-ray (EDX) analysis for Ni and Fe. Figure 3(b) shows spectral data from a line scan across the device showing clear L series peaks for Ni and Fe when focused on the wire. Ni and Fe line profiles are indicated with red and blue lines, respectively, which show these elements upon the structure while none is detected on the substrate within the noise floor of the instrument. The magenta line indicates the energy spectrum captured from the wire, with further detail shown in the upper inset. We note a peak at ~ 1.05 keV, away from the wire, which corresponds to the K series lines of Na. This signal is attributed to a small amount of deposition from the lift-off procedure using NaOH.

Magneto-optical Kerr effect (MOKE) magnetometry was used to characterise the switching in each of the nanowires. An essential requirement in the production of such systems is the realisation of isolated 3D ferromagnetic nanowires, which switch via domain wall motion and with negligible background thin-film upon the substrate. Figure 3(c) shows a magneto-optical Kerr effect magnetometry loop obtained upon a single magnetic nanowire. We observe a loop with coercivity 9 mT and an abrupt transition, indicative of domain wall motion. The use of soft injection pads has previously been used in 2D nanowires in order to inject domain walls controllably, but this has not been explored for 3D systems. Figures 3(d) and 3(e) show MOKE loops obtained on a wire with a 3D nanostructured injection pad. Measurement of the pad yields a rounded loop with a coercivity of ~ 0.5 mT (Fig. 3(d)). Moving the laser spot to the opposite side of the wire yields a loop with a sharp transition and coercivity of just 1 mT (Fig. 3(e)), demonstrating controlled domain wall (DW) injection into the nanowire. Moving the laser spot away from the structures yields no magnetic signal (Fig. S2 in the ESM), further indicating the lift-off procedure has been successful.

With proof-of-principle demonstrated, we move on to extend our methodology to more complex 3DASI structures, which take
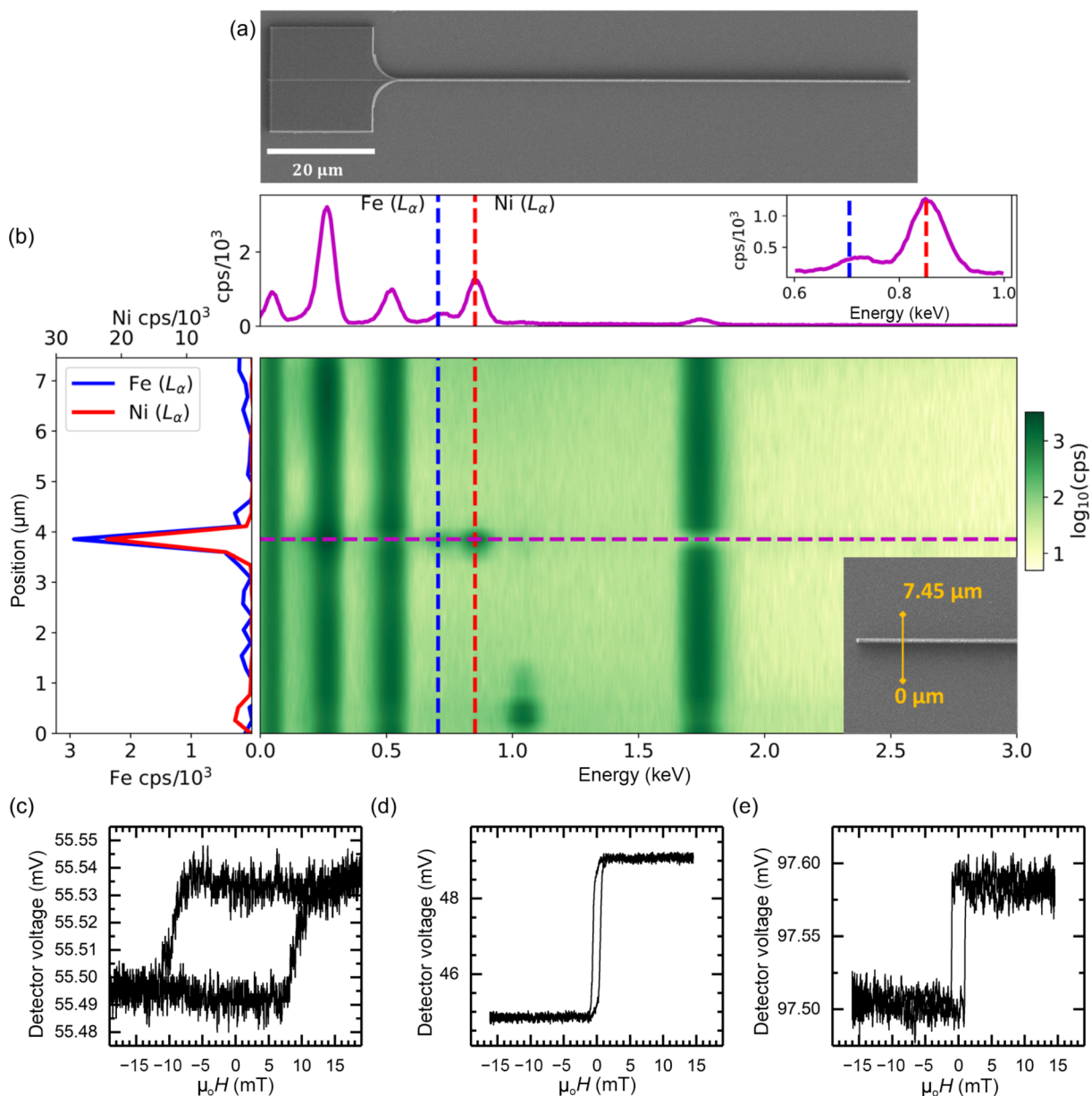

Figure 3 (a) SEM image of a 3D magnetic nanowire with a domain wall injection pad. (b) Spectrogram showing peaks for Ni, Fe, and Na as a function of position. Inset: SEM showing the section of nanowire from which spectrogram was obtained. (c) MOKE loops obtained for a single nanowire without a domain wall injection pad. (d) MOKE loop obtained upon wire with injection pad, with laser focussed upon the pad. (e) MOKE loop obtained upon wire with injection pad, with laser focussed upon the wire.

the form of a diamond lattice geometry [6, 24, 25]. Previous work has shown that sheet film from beyond the system boundaries produces a spurious signal in the magnetometry, which may mask the switching behaviour of the lattice. A further challenge in 3DASI systems is to separate switching from sub-lattices positioned at different depths. Due to the geometry of a diamond bond lattice, with projections of nanowires laying along perpendicular axes, one approach to studying depth dependent switching is by harnessing MOKE. Figure 4(a) shows a schematic of a 3DASI diamond-bond lattice unit cell, with nanowire sub-lattices highlighted by colour. In the experimental MOKE geometry, the wavevector is incident at an angle of ~ 45° with respect to the substrate, with projection along the L1 sub-lattice. There are three distinct MOKE effects which can measure different magnetisation components with respect to the incident k-vector [26], and in the experimental geometry, each of these is present, as depicted in inset of Fig. 4(a). When using an s-polarised incident beam, a longitudinal and polar signal will be present for low analyser angles, which should vanish at an analyser angle of 90°. When harnessing p-polarised light, a low analyser angle again yields a signal where the longitudinal and polar responses are dominant. However, increasing the analyser angle to 90° now isolates the transverse MOKE signal, which yields only a change in intensity and in our experimental geometry should be primarily sensitive to the magnetisation component along the L2 sub-lattice, which is at a lower depth. Hence in principle, polarised light at a low analyser angle should primarily be sensitive to the L1 sub-lattice switching, whereas p-polarised light, at an analyser angle of 90° should primarily be sensitive to the L2 sub-lattice switching, providing a means of obtaining depth dependent switching information.

A large 180 μm × 180 μm area of PAA was ablated away, and a diamond-bond lattice of nanowires was written, subject to a 50 nm $Ni_{81}Fe_{19}$ deposition and lift-off. Two-photon lithography fabrication parameters were identical to those used previously [6, 24], yielding a diamond bond lattice with individual nanowires of width 250 nm and length 1 micron. The overall array size was 180 μm × 180 μm × 10 μm. Our previous work has shown nanowire dimensions upon each sub-lattice agree to within 10% [6].

Figure 4(b) shows a scanning electron micrograph of the resultant structure, with the various sub-lattices labelled. Prior work showed optical magnetometry with signals originating from the sheet film beyond the boundaries of the lattice [6]. With the background film removed, we now carry out a preliminary exploration of the switching within this 3DASI system. Figure 4(c) shows a hysteresis loop obtained in s-polarisation with the field applied in the plane of the substrate, along the projection of the L1 lattice, and with the analyser angle set to ~ 3° from extinction. No

evidence of sheet film switching at low fields is observed, demonstrating our sacrificial layer process has again been successful. With this milestone in place, we proceed to p-polarised light to determine if longitudinal and transverse signals now provide a means to probe sub-lattices of different depths. At a low analyser angle, the measured loop closely resembles the data from the s-polarisation as expected (Fig. S3 in the ESM). Moving to an analyser angle of 90° provides a loop of a very different shape and a sharp transition at approximately 35 mT (Fig. 4(d)). The measurements show differences in signal-to-noise ratio at different analyser angles (signal-to-noise ratio (SNR) ≈ 17 at 3°, and SNR ≈ 4.5 at 90°). This is expected since intensity noise increases significantly with analyser angle [26].

In order to understand the features within the optical magnetometry, micromagnetic simulations were carried out whereby bipod structures were simulated in the experimental field geometries. We note that since the simulations were carried out at zero Kelvin, a systematic difference in coercivity is observed when compared to experimental results, as observed previously [27]. We consider both upper bipods found at the tops of L1 (Figs. 5(a) and 5(b)) and lower bipods found at the L1/L2 intersection (Figs. 5(c) and 5(d)). In each case, every vector component of the magnetisation is plotted. For comparison with experimental MOKE geometries, we examine how the magnetisation varies in the field direction (L_N), transverse to the field direction (T_N), and in the polar direction (P_N).

The left panel of Fig. 5(a) shows a loop for upper bipods, which terminate the experimental lattice surface when the field is applied along the projection of the bipod long-axis. The loop shows some coherent rotation at low fields, before an abrupt transition is observed at approximately 40 mT, whereby the magnetisation component along the wire axis switches. The low field rotation is also observed in the transverse component (T_A, Fig. 5(a), middle panel), which slowly increases to a maximum value before abruptly reducing to zero. Figure 5(a), right-panel (P_A), shows the polar component with field applied along the long-axis projection. Sharp transitions (of order 0.001 M_z) are seen around the switching field of ~ 40 mT. The left panel of Fig. 5(b) shows the loop obtained when the field is applied transverse to the long-axis projection. This shows a hard-axis type loop with rotation at low field and small transitions seen at approximately 60 mT. These transitions are also seen in Fig. 5(b), middle panel (T_B), which shows an abrupt change in the component of magnetisation along the wire long axis. Figure S4 in the ESM shows snapshots of the magnetisation before and after these transitions, which occur upon the down sweep from saturation. Herein, at the threshold field of ~ 65 mT, the demagnetising field drives a transition that yields a rotation of the magnetisation and a larger component along the long axis.
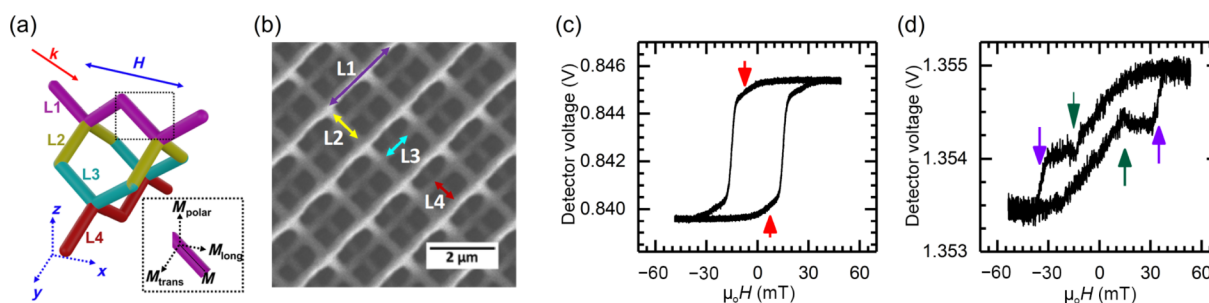

Figure 4 (a) Schematic of experimental MOKE geometry with the 3D artificial spin-ice system. A unit cell of 3DASI is shown, with different sub-lattices depicted. The laser with wavevector k makes an angle of 45° with respect to the substrate and with projection along L1 as depicted. Inset: The magnetisation components that can be measured using the longitudinal, transverse, and polar MOKE effects. (b) Scanning electron microscopy image of 3DASI structure taken at normal incidence. Different sub-lattices are labelled by colour. (c) MOKE loop taken using s-polarised light and with an analyser angle of 3°. (d) MOKE loop taken using p-polarised light and with an analyser angle of 90°.
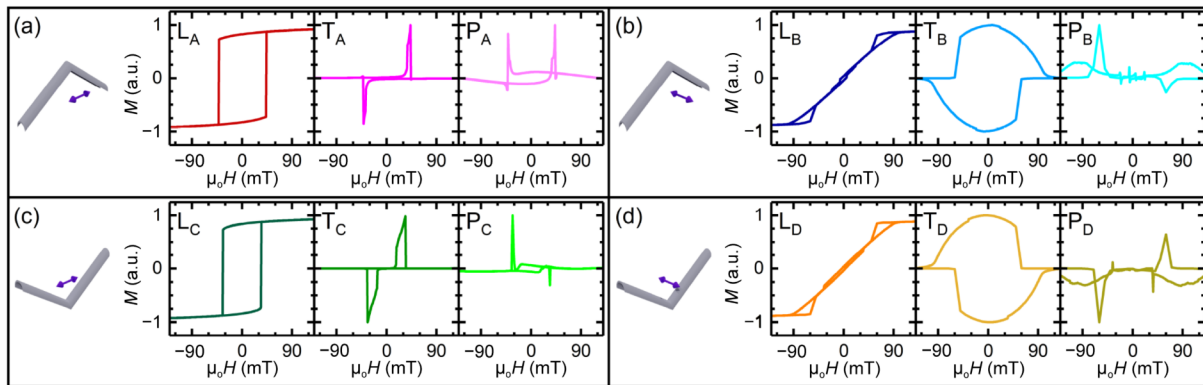
Figure 5 Micromagnetic simulations obtained upon (a) upper bipod system, representative of 3DASI surface termination, with field along the projection of the long-axis; (b) upper bipod system, with field transverse to long-axis projection; (c) lower bipod system with field along the projection of the long-axis; and (d) lower bipod system with field transverse to long-axis projection. For each simulation, the different components of magnetisation are plotted. L_N represents component along field direction, T_N represents component transverse to field direction, and P_N represents component perpendicular to the field direction.

For the experimental data taken at an analyser angle of 3° using p-polarised light (Fig. 4(c)), it is clear that the signal is dominated by the longitudinal component of the uppermost sub-lattice (L1), both of which are reproduced by the simulations in Fig. 5(a) (L_A) and Fig. 5(c) (Lc). We note that the strong rounding in the experimental loop, pre-transition (Fig. 4(c), red arrows), is not captured in L_A or L_C. This suggests that a small contribution from the signal originates from the L2 sub-lattice, with a hard-axis like characteristic as depicted in Fig. 5(b) (L_B). Next, we move on to interpret the transverse experimental loop taken in p-polarised light and at an analyser angle of 90° (Fig. 4(d)). We note immediately that the subtle antisymmetric features (Fig. 4(d), green arrows) are reproduced by the transverse component with field along the long axis as depicted in Fig. 5(a) (T_A) and Fig. 5(c) (T_C). This suggests that this signal is coming from L1, and analysis of the simulated magnetisation profiles suggests it originates from magnetisation rotation at the vertex areas (Fig. S5 in the ESM). We note that any transverse signal at the lower four-way L1/L2 vertex is likely to be more complex though we cannot completely discount the possibility that this area may contribute to the observed asymmetric features. The higher field transition seen in Fig. 4(d) (purple arrows), is not explained easily by any component in the simulations depicted in Fig. 5. The polar loops (P_B in Fig. 5(b) and P_D in Fig. 5(d)) show some transitions at higher fields, but we note that the polar MOKE effect is not present at an analyser angle of 90°. We also note that the absolute change in M_z in such transitions is of order 10^{-3} (Fig. S6 in the ESM). We note that the second transition is also unlikely to be due to pinning upon either sub-lattice. Our previous work has shown that whilst pinning does occur upon L1 and L2 sub-lattices, producing monopole defects [24], the maximum field required to surpass this pinning is approximately 10 mT, well below the additional transition seen within our transverse data. Finally, the transition occurs after saturation along one direction and application of the reverse field, quite unlike the transition seen in Fig. 5(b), middle (T_B).

We note that within our experimental setup, a small angular (~ 5°) misalignment of the field with respect to the L1 projection is possible. Standard models for simple single domain, high aspect ratio systems [28, 29] predict an increased switching field for angles close to 90°. Whilst we note that our 3D system is more complex in geometry, such a dependence would suggest that the transition measured in Fig. 4(d) originates from the L2 sub-lattice. To investigate these transitions, micro-magnetic simulations are carried out upon bipod structures, but with a 5° misalignment of the field (Fig. S7 in the ESM). These show an approximate factor of 2 difference in switching fields for two perpendicular oriented

sub-lattices, consistent with our experimental data. Hence, our analysis shows that MOKE can be used to obtain switching information from different parts of the 3D geometry. We have shown sensitivity to switching that originates from the terminating bipod vertex upon L1, from the length of wires upon the L1 sub-lattice and then from wires present upon the L2 sub-lattice. Overall, we have measured switching from three different depths of the 3DASI lattice.

3 Conclusions

In conclusion, we have demonstrated a novel methodology that utilises 3D lithography with a sacrificial layer in order to cast a complex 3D geometry into a functional material. We show proof-of-principle of this approach by fabricating planar magnetic nanowires raised above the substrate, with injection pads allowing controlled nucleation of domain walls that can be probed optically. Going beyond this, we show that our technique can be used with 3DASI systems and have used optical magnetometry to observe switching upon two sub-lattices of different depths. We envisage our fabrication methodology will have an impact on materials science and physics, allowing the influence of complex 3D geometry upon electronic, optical, and magnetic properties to be investigated.

4 Experimental methods

4.1 Fabrication

22 mm × 22 mm glass coverslips with thickness between 0.16 and 0.19 mm and a 500 nm indium tin oxide (ITO) coating were used for the substrate. After cleaning with acetone and IPA, a 5 wt.% solution of PAA was spin-coated on the ITO face yielding a thickness of ~ 100 nm. Immersion oil (Immersol 518F) was drop-cast upon the bottom face.

The geometry was subsequently ablated into the PAA layer. Herein, a 180 mW, 780 nm laser with a pulse width of 100 fs and repetition rate of 80 MHz was beam expanded to backfill a NA = 1.4, 63× objective, which was subsequently focussed to a diffraction limited spot. A galvo mirror was used to steer the beam and ablate the desired geometry according to a predesigned computer-aided design (CAD) file. A negative resist (IPL-780) was subsequently drop cast onto the PAA face of the sample. The structures were then written into the ablated regions using two-photon lithography, and the resultant samples were developed in propylene glycol monomethyl ether acetate for 20 min to remove any unexposed resists. The samples were then cleaned in IPA and dried with compressed air.

Permalloy ($Ni_{81}Fe_{19}$) was subsequently deposited via thermal evaporation. A 0.03 g ribbon of $Ni_{81}Fe_{19}$ was placed in an alumina evaporation boat, and the evaporation took place with a base pressure below 10^{-6} mbar. For the nanowires, a uniform film with a thickness of 27.5 nm was deposited at $0.1 \text{ nm} \cdot \text{s}^{-1}$. For the 3D artificial spin-ice system, a film thickness of approximately 25 nm was used, deposited at $0.1 \text{ nm} \cdot \text{s}^{-1}$.

After evaporation, the samples were placed in a bath of $0.5 \text{ mol} \cdot \text{L}^{-1}$ NaOH solution to dissolve the PAA layer and lift the substrate film off the sample. To reduce the surface tension, which may damage the structures when removing the sample from the bath, the water was displaced with IPA, and the samples were subsequently air-dried using compressed air.

4.2   Simulations

The code NMAG [30] was used to perform the micromagnetic simulations using material parameters for $Ni_{81}Fe_{19}$ with a saturation magnetisation of $M_s = 0.86 \times 10^6 \text{ A} \cdot \text{m}^{-1}$ and exchange stiffness of $A = 13 \times 10^{-12} \text{ J} \cdot \text{m}^{-1}$ resulting in an exchange length of $\Delta_{ex} \approx 5.2$ nm. The geometries were meshed with a minimum mesh size of 2 nm and a maximum of 5 nm.

4.3   MOKE

A 100 mW, 637 nm wavelength laser attenuated to 5 mW was polarised into s- or p-light using a Glan Taylor polariser. The beam was expanded and then focused using an achromatic doublet with a focal length $f = 10$ cm to obtain a spot size of approximately 10 μm². In the case of the 3DASI lattices, the focal spot was positioned in the centre of the lattice to avoid contributions due to symmetry breaking at the lattice edge. To measure the longitudinal and polar effects in s- and p-polarisation, the reflected beam was passed through a second Glan–Taylor analyser which was set to 3° from extinction, for which the transmitted beam was directed onto an amplified Si photodetector to generate the Kerr signal. In order to measure the transverse MOKE effect, the analyser was either entirely removed or aligned with the original polariser. Both yielded similar signals with only a difference in signal magnitude, as expected. For measurements of the nanowire system, k was directed to maximise the projection along the long axis. For measurements of the 3DASI diamond lattice system, k was aligned to maximise projection along the uppermost (L1) lattice.

Acknowledgements

Electronic Supplementary Material: Supplementary material (AFM, MOKE, and finite element simulations) is available in the online version of this article at https://doi.org/10.1007/s12274-022-4649-z.

References

[1] Skylar-Scott, M. A.; Mueller, J.; Visser, C. W.; Lewis, J. A. Voxelated soft matter via multimaterial multinozzle 3D printing. *Nature* **2019**, *575*, 330–335.

[2] Elder, B.; Neupane, R.; Tokita, E.; Ghosh, U.; Hales, S.; Kong, Y. L. Nanomaterial patterning in 3D printing. *Adv. Mater.* **2020**, *32*, 1907142.

[3] Bauer, J.; Schroer, A.; Schwaiger, R.; Kraft, O. Approaching theoretical strength in glassy carbon nanolattices. *Nat. Mater.* **2016**, *15*, 438–443.

[4] Gernhardt, M.; Blasco, E.; Hippler, M.; Blinco, J.; Bastmeyer, M.; Wegener, M.; Frisch, H.; Barner‑Kowollik, C. Tailoring the mechanical properties of 3D microstructures using visible light post-manufacturing. *Adv. Mater.* **2019**, *31*, 1901269.

[5] Kadic, M.; Milton, G. W.; Van Hecke, M.; Wegener, M. 3D metamaterials. *Nat. Rev. Phys.* **2019**, *1*, 198–210.

[6] May, A.; Hunt, M.; Van Den Berg, A.; Hejazi, A.; Ladak, S. Realisation of a frustrated 3D magnetic nanowire lattice. *Commun. Phys.* **2019**, *2*, 13.

[7] Kern, C.; Kadic, M.; Wegener, M. Experimental evidence for sign reversal of the hall coefficient in three-dimensional metamaterials. *Phys. Rev. Lett.* **2017**, *118*, 016601.

[8] Cao, Y. Y.; Takeyasu, N.; Tanaka, T.; Duan, X. M.; Kawata, S. 3D metallic nanostructure fabrication by surfactant-assisted multiphoton-induced reduction. *Small* **2009**, *5*, 1144–1148.

[9] Bernardeschi, I.; Ilyas, M.; Beccai, L. A review on active 3D microstructures via direct laser lithography. *Adv. Intell. Syst.* **2021**, *3*, 2100051.

[10] Hunt, M.; Taverne, M.; Askey, J.; May, A.; Van Den Berg, A.; Ho, Y. L. D.; Rarity, J.; Ladak, S. Harnessing multi-photon absorption to produce three-dimensional magnetic structures at the nanoscale. *Materials* **2020**, *13*, 761.

[11] Harinarayana, V.; Shin, Y. C. Two-photon lithography for three-dimensional fabrication in micro/nanoscale regime: A comprehensive review. *Opt. Laser Technol.* **2021**, *142*, 107180.

[12] Puce, S.; Sciurti, E.; Rizzi, F.; Spagnolo, B.; Qualtieri, A.; De Vittorio, M.; Staufer, U. 3D-microfabrication by two-photon polymerization of an integrated sacrificial stencil mask. *Micro Nano Eng.* **2019**, *2*, 70–75.

[13] Liao, P.; Xing, L. X.; Zhang, S. W.; Sun, D. Magnetically driven undulatory microswimmers integrating multiple rigid segments. *Small* **2019**, *15*, 1901197.

[14] Fernández-Pacheco, A.; Streubel, R.; Fruchart, O.; Hertel, R.; Fischer, P.; Cowburn, R. P. Three-dimensional nanomagnetism. *Nat. Commun.* **2017**, *8*, 15756.

[15] Askey, J.; Hunt, M. O.; Langbein, W.; Ladak, S. Use of two-photon lithography with a negative resist and processing to realise cylindrical magnetic nanowires. *Nanomaterials* **2020**, *10*, 429.

[16] Sahoo, S.; Mondal, S.; Williams, G.; May, A.; Ladak, S.; Barman, A. Ultrafast magnetization dynamics in a nanoscale three-dimensional cobalt tetrapod structure. *Nanoscale* **2018**, *10*, 9981–9986.

[17] Williams, G.; Hunt, M.; Boehm, B.; May, A.; Taverne, M.; Ho, D.; Giblin, S.; Read, D.; Rarity, J.; Allenspach, R. et al. Two-photon lithography for 3D magnetic nanostructure fabrication. *Nano Res.* **2018**, *11*, 845–854.

[18] Parkin, S. S. P.; Hayashi, M.; Thomas, L. Magnetic domain-wall racetrack memory. *Science* **2008**, *320*, 190–194.

[19] Parkin, S.; Yang, S. H. Memory on the racetrack. *Nat. Nanotechnol.* **2015**, *10*, 195–198.

[20] Sanz-Hernández, D.; Hamans, R. F.; Liao, J. W.; Welbourne, A.; Lavrijsen, R.; Fernández-Pacheco, A. Fabrication, detection, and operation of a three-dimensional nanomagnetic conduit. *ACS Nano* **2017**, *11*, 11066–11073.

[21] Linder, V.; Gates, B. D.; Ryan, D.; Parviz, B. A.; Whitesides, G. M. Water-soluble sacrificial layers for surface micromachining. *Small* **2005**, *1*, 730–736.

[22] Kumagai, H.; Midorikawa, K.; Toyoda, K.; Nakamura, S.; Okamoto, T.; Obara, M. Ablation of polymer films by a femtosecond high-peak-power Ti: sapphire laser at 798 nm. *Appl. Phys. Lett.* **1994**, *65*, 1850–1852.

[23] Rethfeld, B.; Ivanov, D. S.; Garcia, M. E.; Anisimov, S. I. Modelling ultrafast laser ablation. *J. Phys. D:Appl. Phys.* **2017**, *50*, 193001.

[24] May, A.; Saccone, M.; Van Den Berg, A.; Askey, J.; Hunt, M.; Ladak, S. Magnetic charge propagation upon a 3D artificial spin-ice. *Nat. Commun.* **2021**, *12*, 3217.

[25] Sahoo, S.; May, A.; Van Den Berg, A.; Mondal, A. K.; Ladak, S.; Barman, A. Observation of coherent spin waves in a three-dimensional artificial spin ice structure. *Nano Lett.* **2021**, *21*, 4629–4635.

[26] Allwood, D. A.; Xiong, G.; Cooke, M. D.; Cowburn, R. P. Magneto-optical kerr effect analysis of magnetic nanostructures. *J. Phys. D:Appl. Phys.* **2003**, *36*, 2175–2182.

[27] Ladak, S.; Read, D. E.; Perkins, G. K.; Cohen, L. F.; Branford, W. R. Direct observation of magnetic monopole defects in an artificial spin-ice system. *Nat. Phys.* **2010**, *6*, 359–363.

[28] Kondorsky, E. On hysteresis in ferromagnetics. *J. Phys.* **1940**, *2*, 161–181.

[29] Fernández-Pacheco, A.; Serrano-Ramón, L.; Michalik, J. M.; Ibarra, M. R.; De Teresa, J. M.; O'Brien, L.; Petit, D.; Lee, J.; Cowburn, R. P. Three dimensional magnetic nanowires grown by focused electron-beam induced deposition. *Scientific Reports* **2013**, *3*, 1492.

[30] Fischbacher, T.; Franchin, M.; Bordignon, G.; Fangohr, H. A systematic approach to multiphysics extensions of finite-element-based micromagnetic simulations: Nmag. *IEEE Trans. Magn.* **2007**, *43*, 2896–2898.